Advances in Water Resources 105 (2017) 82–95

Contents lists available at ScienceDirect

Advances in Water Resources

journal homepage: www.elsevier.com/locate/advwatres

Multiscale modelling of dual-porosity porous media; a computational pore-scale study for flow and solute transport

Enno T. de Vries[a], Amir Raoof[a,*], Martinus Th. van Genuchten[a,b]

[a] Department of Earth Sciences, Utrecht University, Utrecht, The Netherlands
[b] NIDES Interdisciplinary Center for Social Development, Federal University of Rio de Janeiro, Rio de Janeiro, Brazil

ARTICLE INFO

Article history:
Received 8 December 2016
Revised 18 April 2017
Accepted 19 April 2017
Available online 20 April 2017

Keywords:
Pore network model
Aggregated soil
Dual-porosity
Solute transport
Mobile-immobile transport model

ABSTRACT

Many environmental and agricultural applications involve the transport of water and dissolved constituents through aggregated soil profiles, or porous media that are structured, fractured or macroporous in other ways. During the past several decades, various process-based macroscopic models have been used to simulate contaminant transport in such media. Many of these models consider advective-dispersive transport through relatively large inter-aggregate pore domains, while exchange with the smaller intra-aggregate pores is assumed to be controlled by diffusion. Exchange of solute between the two domains is often represented using a first-order mass transfer coefficient, which is commonly obtained by fitting to observed data. This study aims to understand and quantify the solute exchange term by applying a dual-porosity pore-scale network model to relatively large domains, and analysing the pore-scale results in terms of the classical dual-porosity (mobile-immobile) transport formulation.

We examined the effects of key parameters (notably aggregate porosity and aggregate permeability) on the main dual-porosity model parameters, i.e., the mobile water fraction (ϕ_m) and the mass transfer coefficient (α). Results were obtained for a wide range of aggregate porosities (between 0.082 and 0.700). The effect of aggregate permeability was explored by varying pore throat sizes within the aggregates. Solute breakthrough curves (BTCs) obtained with the pore-scale network model at several locations along the domain were analysed using analytical solutions of the dual-porosity model to obtain estimates of ϕ_m and α. An increase in aggregate porosity was found to decrease ϕ_m and increase α, leading to considerable tailing in the BTCs. Changes in the aggregate pore throat size affected the relative flow velocity between the intra- and inter-aggregate domains. Higher flow velocities within the aggregates caused a change in the transport regime from diffusion dominated to more advection dominated. This change increased the exchange rate of solutes between the mobile and immobile domains, with a related increase in the value of the mass transfer coefficient and less tailing in the BTCs.

1. Introduction

Soil and groundwater pollution by a broad range of industrial and agricultural contaminants is an ever-increasing problem worldwide. One issue exacerbating effective management of the subsurface is the problem of preferential flow of surface applied chemicals such as fertilizers, pesticides, trace elements and pathogenic microorganisms. Much evidence exists that preferential flow through especially the vadose zone is contributing to surface and subsurface pollution problems (e.g., Flury et al., 1994; Abbaspour et al., 2001; Hendrickx and Flury, 2001; Allaire et al., 2009, Vogel et al., 2010; Zhang et al., 2013; Mahmoodlu et al., 2013, 2014). In attempts to describe and quantify the basic processes leading to preferential flow, a large number of dual-porosity, dual-permeability, multi-porosity and multi-permeability models and related approaches have been developed and verified. Comprehensive reviews of alternative modelling approaches are provided by NRC (2001), Šimůnek et al. (2003), Gerke (2006), Jarvis (2007), Šimunek and van Genuchten (2008) and Köhne et al. (2009).

A commonality of many preferential flow models is the assumption that the liquid phase can be divided into relatively mobile and immobile parts representing the macropore (or inter-aggregate or fracture) domain, and the micropore (or intra-aggregate or soil matrix) domain, respectively, together with appropriate coupling terms to account for the exchange of water and/or dissolved constituents between the two domains. The simplest formulation arises when no flow occurs in the micropore domain, and a first-order macropore/micropore solute exchange

* Corresponding author.
E-mail address: a.raoof@uu.nl (A. Raoof).

http://dx.doi.org/10.1016/j.advwatres.2017.04.013

term is used, to lead to mobile-immobile (MIM) type dual-porosity models of the form (Coats and Smith, 1964; van Genuchten and Wierenga, 1976):

$$\phi_m \theta \frac{\partial \bar{c}_m}{\partial t} = \phi_m \theta D_m \frac{\partial^2 \bar{c}_m}{\partial x^2} - q \frac{\partial \bar{c}_m}{\partial x} - \alpha (\bar{c}_m - \bar{c}_{im}) \quad (1)$$

$$(1 - \phi_m)\theta \frac{\partial \bar{c}_{im}}{\partial t} = \alpha (\bar{c}_m - \bar{c}_{im}) \quad (2)$$

where the subscripts m and im refer to the mobile and immobile region, $\bar{c}$ is the average concentration, θ is the volumetric water content, ϕ_m is the mobile water fraction defined as θ_m/θ, D_m is the dispersion coefficient, q is the volumetric fluid flux, and α is a first-order mass transfer coefficient.

The dual-porosity model given by Eqs. (1) and (2) involves several assumptions, the most important being that advective transport in the smaller intra-aggregate pores can be neglected. This implies that the overall pore water velocity distribution within the porous medium is approximated by the step function, with one part of the medium having an average pore water velocity equal to $v_m = q/\theta_m$, while water in the other part is completely stagnant. This assumption is generally not met since the intra-aggregate (soil matrix) region often has some non-zero permeability, even if small compared to the inter-aggregate (or fracture) region.

Another simplifying assumption of Eqs. (1) and (2) is that solute exchange between the mobile and immobile regions can be described using a quasi-empirical first-order rate term proportional to the difference between the average concentrations of the mobile and immobile regions. Various attempts have been made to obtain a more physical basis of the mass transfer coefficient, α, in terms of such parameters as the diffusion coefficient and the shape and size of the aggregates or soil matrix. This has led to a number of analytical models that explicitly considered diffusion from the inter-aggregate region into immobile intra-aggregate regions of various shapes (e.g., Rasmuson and Neretnieks, 1980; Tang et al., 1981; Sudicky and Frind, 1982; van Genuchten et al., 1984; van Genuchten, 1985). These and related studies also allowed derivation of approximate relationship for the mass transfer coefficient, including through the use of Laplace transforms or moment analyses, as exemplified in studies by van Genuchten and Dalton (1986), Bolt (1979), Barker (1985), van Genuchten and Dalton (1985), Parker and Valocchi (1986), Goltz and Roberts (1987), and Hantush and Marino (1988).

Another approach for estimating the parameters ϕ_m and α in Eqs. (1) and (2) is by direct measurement (e.g., Clothier et al., 1992; Jaynes and Shao, 1999), or by analyzing a large number of previously published data such as shown by Maraqa (2001). A latter study revealed an approximately linear relationship between the mass transfer coefficient and the residence time of the solute in the transport domain (Pontedeiro et al., 2010).

Both of the above assumptions (i.e., negligible advection within the aggregates, and the use of a first-order exchange term) require more research. This includes how best to account for aggregate shape and size, which are known to vary widely and may involve various spherical, blocky, columnar, and prismatic geometries, or mixtures thereof (e.g., Tisdall and Oades, 1982; Hillel, 2003). Imaging techniques can be of great value for determining the size and shapes of aggregates, and hence can reduce the dependency on using idealized shapes (Bultreys et al., 2015, 2016). The mass transfer coefficient is, in actuality, a more complex integrated parameter whose value depends on many porous media characteristics including pore and aggregate geometry, the solute diffusion coefficient, the intra-aggregate permeability, the relative magnitude of the mobile and immobile region, as well as the dynamics of the overall system such as the concentration gradients and the applied flow velocity. At relatively low pore water velocities, the time scale of solute diffusion into aggregates may be comparable with the transport time scale within the macropore domain, in which case a larger fraction of the solutes may diffuse into or out of the aggregates, thus limiting any tailing in observed BTCs. At the other extreme, at relatively high pore water velocities, macro- and micro-pores may become essentially disconnected, leading to negligible solute exchange and possibility of dual peaks in the BTCs (Zhou et al., 2014).

The value of the mass transfer coefficient, α, is commonly obtained by fitting macroscopic models to observed solute BTCs (Toride et al., 1995). Since BTCs often show tailing, this approach may be very time-consuming in terms of getting appropriate resolution in the data. Moreover, the BTC data then provide information only of the macroscopic concentrations at selected observation points within the medium, or from column outflow experiments, thus providing little insight into the internal concentration distributions and interactions between the mobile and immobile zones. This makes it difficult to estimate contribution of different transport processes into the BTCs and extrapolate such BTC data to other transport regimes. Methods are hence needed to provide information in a systematic manner about the internal state of aggregated media, including quantification of the basic transport processes operating at the microscopic level. An alternative would be to obtain the BTCs using pore scale modelling (Raoof et al., 2010; Raoof and Hassanizadeh, 2013). For transport in unsaturated non-aggregated media, Raoof and Hassanizadeh (2013) used pore network modelling to obtain several BTCs in this manner, which would be difficult and time consuming to obtain experimentally.

Advanced 3D X-ray microtomography and related imaging techniques are now being increasingly used to obtain non-destructive visualizations of pore structures (Allaire et al., 2009; Dal Ferro et al., 2013; Mangalassery et al., 2013; Zhou et al., 2013; Martínez et al., 2015). This includes studies of dynamic processes such as fluid flow and structural dynamic processes (Cnudde and Boone, 2013; Wildenschild and Sheppard, 2013). Soil aggregates for such studies could be imaged and analysed individually to collect data on pore morphology and connectivity (Zhou et al., 2013; Dal Ferro et al., 2013), or direct fluid flow experiments could be performed on a dual-porosity medium. Resulting information can then be utilized to construct pore network structures needed for pore-scale flow and/or transport models.

Various pore-scale modelling approaches are now being pursued, with differences pertaining to the specific mathematical formulation such as the use of direct numerical solutions (Bijeljic et al., 2013; Fathi et al., 2017a, 2017b), Lattice Boltzmann methods (Jafari et al., 2011) or pore network modelling (Raoof et al., 2013), including differences in the invoked modelling resolution and required computational time (Sahimi, 2011; Bultreys et al., 2016). Multi-scale pore network modelling have been applied for simulating two-phase flow (Bultreys et al., 2015; Jiang et al., 2013; Prodanović et al., 2015) as well as solute transport (Bijeljic et al., 2013). and also using grain filling and pore filling method (Mehmani and Prodanović, 2014).

The aim of our study was to use a pore-scale network model to simulate flow and transport in dual-porosity domains containing a large number of aggregates. The pore network modelling approach assumes that the porous medium continuum can be divided into pore elements made up of pore bodies representing the larger voids in the medium, and pore throats representing narrow openings connecting the pore bodies (Raoof et al., 2013; Bultreys et al., 2016). Applying mass balance equations, flow and transport is simulated within each individual pore. Averaging over a large number of pores will then allow estimation of the macroscopic transport properties for porous media containing unimodal pore sizes (Raoof et al., 2010, 2013), or for multi-scale media with multimodal pore size distributions (Bultreys et al., 2015; Mehmani and Prodanović, 2014; Mehmani et al., 2015). The obtained information at the

pore-scale makes it possible to relate macroscopic transport properties to the underlying physical pore-scale processes and pore size distributions, and their connectivities (Raoof et al., 2010; Raoof and Hassanizadeh, 2013). Using such multi-scale porous media requires description of the connectivity between the macro- and micro-porosity domains, which computationally can be particularly challenging for heterogeneous multimodal pore scale domains.

Our objective is to develop a dual-porosity pore structure to represent an aggregated medium, and to use this structure to simulate flow and transport within the composite medium in order to obtain pore-scale distributions of the solute concentration. The resulting solute breakthrough curves are then compared with solutions of the macroscopic equations given by Eqs (1) and (2) to obtain estimates of the fraction of mobile water (ϕ_m), and the mass transfer coefficient (α). A large number of simulations will be carried out to obtain dependencies of ϕ_m and α on such soil aggregate properties as porosity and internal permeability. Resulting insight may be useful for field scale models to improve predictions needed at the larger scales for evaluating alternative management or contaminant remediation strategies, as well as industrial porous media applications.

2. Theoretical development

In this section we describe the pore-scale network model that was used to simulate flow and transport in the aggregated dual-porosity pore structure. After a brief review of the pore-scale network modelling approach in general, details are provided on how the pore-scale model was used to generate pore structures and conduct simulations for an aggregated medium.

2.1. Pore network model

Pore network modelling considers a porous medium as a system of pore elements composed of pore bodies and pore throats. While pore bodies, due to their larger size, mainly control the porosity of the medium, the smaller pore throats determine the hydraulic conductivity. The complete pore structure of an aggregated soil requires the use of two types of pore spaces with different sizes. The aggregated medium in our study was obtained by first generating a macropore domain. Since pore connectivity is an important topological property of the medium, we used a pore network model with random pore connectivity (Raoof & Hassanizadeh, 2012) to represent the randomness of real porous media. Once the macropore domain was generated, several aggregates were superimposed within the overall domain. Each aggregate of certain size was assumed to contain a large number of micropores. Algorithms were developed to connect the collection of pores located at the outer surface of the aggregates to their adjacent macropores. We generated for this purpose several domains with different aggregate fractions, with the aggregates themselves randomly placed within the medium. An example is shown in Fig. 1. Once the pore structures were constructed, flow and transport processes were simulated within the pore network domain using the PoreFlow package developed by Raoof et al., (2013), which is capable of simulating saturated and variably-saturated flow, as well as multi-component reactive transport, within arbitrary pore structures.

Since the adopted pore-scale model has been explained in detail elsewhere (Raoof and Hassanizadeh, 2010, 2012; Raoof et al., 2010, 2013), only a brief overview is provided here of the main equations governing flow and transport within the porous medium. Assuming laminar flow, the volumetric flow rate within each pore was obtained using the Hagen-Poiseulle equation:

$$q_{ij} = g_{ij}\left(p_j - p_i\right) \tag{3}$$

where q_{ij} is the volumetric volume rate through the pore throat between two adjacent connected pore bodies i and j, p_i and p_j are pressures of the two adjacent pore bodies, and g_{ij} is the conductance of the pore throat which, for a pore throat with a cylindrical cross section, is given by:

$$g_{ij} = \frac{\pi R_{ij}^4}{8\mu l_{ij}} \tag{4}$$

where R_{ij} is the pore throat radius, l_{ij} is the throat length, and μ is the fluid dynamic viscosity.

Considering incompressible flow, the continuity equation for flow is applied at pore junctions:

$$\sum_{j=1}^{z_i} q_{ij} = 0; \qquad j = 1, 2, \ldots, z_i, \tag{5}$$

where q_{ij} is the volumetric flow rate within a pore throat from pore body i to pore body j, and z_i is the pore coordination number of pore i.

Combining Eqs. (3)–(5) for all pores results in a linear system of equations with a sparse, symmetric and positive-definite coefficient matrix, which is to be solved for the pore body pressures. Considering the sample as a representative elementary volume (REV), the average pore water velocity, $\bar{v}$, can be calculated as (Raoof et al., 2013):

$$\bar{v} = \frac{Q_{tot} L}{V_f} \tag{6}$$

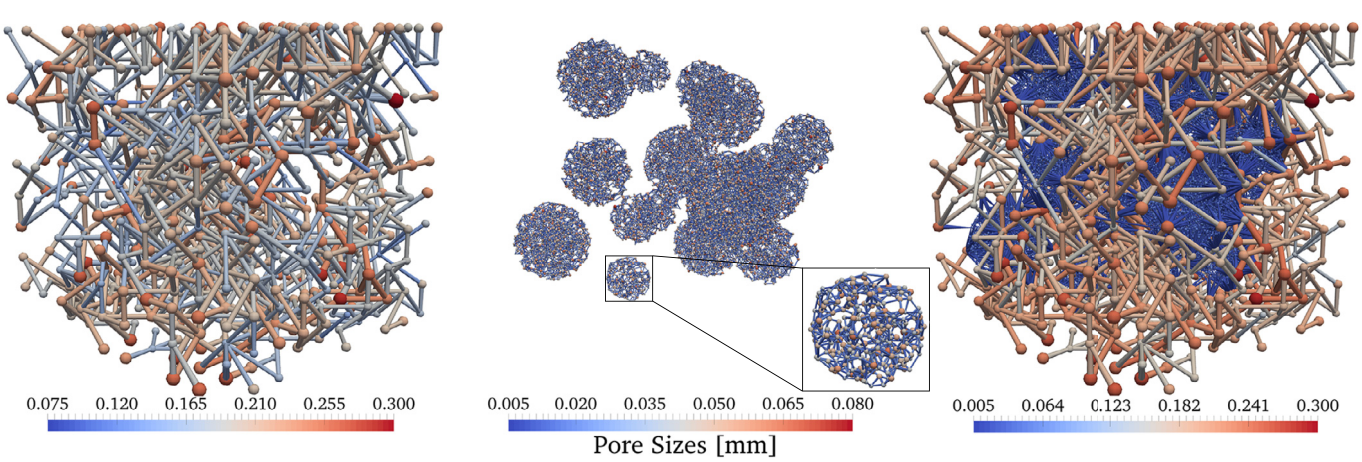

Fig. 1. Construction of the aggregated domain: macroscopic pore domain (the left plot) as well as the aggregate domain (the middle plot) are created and superimposed to provide the ultimate multi-scale domain (the right plot).

Table 1
Selected literature on aggregate properties: aggregate diameters, pore sizes, and porosities.

Reference	Aggregate diameter (mm)	Pore size (μm)	Mean aggregate porosity [–]	Imaging method
Czachor et al. (2015)	3–4	2.5–100	0.35	X-ray microtomography and paraffin intrusion
Dal Ferro et al. (2012)	1–2	0.074–100	0.37	X-ray microtomography and mercury intrusion
Dal Ferro et al. (2013)	5–6	12.5–200	0.11	X-ray microtomography
Khan et al. (2012)	1–5	1–85	0.40	Synchrotron-based nano-CT
Peth et al. (2008)	3–5	5–50	0.13	X-ray microtomography
Rabbi et al. (2015)	2–4	5.2–60	0.048	X-ray microtomography
Zhou et al. (2013)	1.5–2	10–500	0.14	X-ray microtomography

where Q_{tot} is the total discharge rate through the pore network, which can be determined at the inlet or outlet of the pore network as the sum of all fluxes, L is the length of the pore network, and V_f is the total volume of the fluid phase within the pore network.

The intrinsic permeability, κ, of the sample can be determined using Darcy's law:

$$\kappa = \frac{\mu Q_{tot} L}{A\ \Delta P} \tag{7}$$

where μ is the dynamic viscosity, ΔP is the pressure difference between the inlet and outlet pores, and A is the cross-sectional area of the pore network.

Solute transport through the pore network was described for the general case involving both advective transport and diffusion (Vasilyev et al., 2012). Calculations were done by considering each pore element (i.e., a pore body or a pore throat) as the control volume. We used a backward Euler method for the temporal discretization and first-order upwind and central schemes for spatial discretization of the advection and diffusion terms, respectively. For a given pore body i, one can write the following mass balance equation:

$$V_i \frac{dc_i}{dt} = \sum_{j=1}^{N_{in}^{throat}} q_{ij} c_{ij} - Q_i c_i + \sum_{j=1}^{z_i} D_0 A_{ij} \frac{(c_{ij} - c_i)}{l_{ij}}, \tag{8}$$

where V_i is the volume of the pore body, Q_i is the total volumetric rate going out of the pore body, A_{ij} is the cross-sectional area of the pore throat, D_0 is the ionic or molecular diffusion coefficient, c_i is the concentration in the pore body, c_{ij} is the concentration in the pore throat, l_{ij} is again the length of the throat, while N_{in}^{throat} represents the number of pore throats flowing into pore body i.

Similarly, the mass balance equation for solutes in a pore throat ij may be written as:

$$V_{ij} \frac{dc_{ij}}{dt} = q_{ij} c_j - q_{ij} c_{ij} + D_0 A_{ij} \frac{(c_j - c_{ij})}{l_{ij}} + D_0 A_{ij} \frac{(c_i - c_{ij})}{l_{ij}} \tag{9}$$

which assumes that pore body j is the upstream node. Eqs. (8) and (10) were solved using a fully implicit scheme available in the PoreFlow software package (Raoof et al., 2013). Flux-averaged breakthrough curves at selected points were obtained by averaging concentrations over the network cross-section at successive times as follows:

$$c(x,t) = \left[\frac{\sum_i^{N_t^x} c_i(x,t) Q_i}{\sum_i^{N_t^x} Q_i} \right] \frac{1}{c_0} \qquad i = 1, 2, \ldots, N_t \tag{10}$$

where $c(x,t)$ is the normalized average concentration at location x and time t, N_t^x refers to the total number of pores at location x, and c_0 is the input concentration of the solute.

2.2. Application to aggregated media

Imaging techniques such as X-ray microtomography are being increasingly used to visualize the inner structures of aggregates and to provide information on pore size distribution, aggregate porosity, and aggregate size and shape (Mangalassery et al., 2013; Martínez et al., 2015; Zhou et al., 2013; Dal Ferro et al., 2013). We note that studies using only X-ray microtomography often show lower aggregate porosities as compared to studies using multiple measuring techniques (Czachor et al., 2015; Dal Ferro et al., 2012, 2013). The resolution of X-ray tomography has been shown to be a limiting factor since it tends to neglect the presence of below-resolution pores. Additional techniques such as mercury intrusion hence are often used to obtain a more realistic value for the porosity of the aggregates (Dal Ferro et al., 2013). Focused ion beam-scanning electron microscopy (FIB-SEM) can provide much higher resolution images, as compared to X-ray tomography, for analysing microporosity (Hemes et al., 2015). Using a combination of multiple techniques applicable to different scales will be most valuable for multi-scale pore topology applications such as in this study. Table 1 shows aggregate sizes, pore sizes and aggregate porosities as obtained from the literature. We used these data to establish as realistic ranges of properties as possible for the aggregates used in our calculations.

Transport processes within the aggregated media we considered were studied by first creating a reference model. The reference model was then modified to consider i) domains with different aggregate porosities by changing pore body sizes, and ii) domains with different aggregate permeabilities by changing pore throat sizes to explore the effects of flow velocity differences between the macro- and aggregate domains. The reference model had a physical size of $100 \times 20 \times 20\,\text{mm}^3$ and contained a total of 1000 aggregates. The mean distance between pore bodies in the aggregates was taken to be 0.1 of the separation distance between the macropores, while the mean coordination number was taken to be 5. The minimum and maximum aggregate diameters were set to 1.0 and 3.0 mm, respectively. Pore body sizes and aggregate throat sizes were assigned from a truncated log-normal distribution given by (Raoof & Hassanizadeh, 2012).

$$f(R_i, \sigma) = \frac{\sqrt{2} exp\left[-\left(\frac{1}{2}\right) \left[\ln\left(\frac{R_i}{R_m}\right) / \sigma \right]^2 \right]}{\sqrt{\pi \sigma^2} R_i \left\{ erf\left[\ln\left(\frac{R_{max}}{R_m}\right) / \sqrt{2\sigma^2} \right] - erf\left[\ln\left(\frac{R_{min}}{R_m}\right) / \sqrt{2\sigma^2} \right] \right\}} \tag{11}$$

where R_{min}, R_{max} and R_m are the minimum, maximum and mean of the distribution, and σ^2 is the variance of the distribution. The macropore and micropore bodies each had their own size distribution. The macropore throat sizes were set as the smallest of the adjacent pore body sizes. The throat lengths were calculated by determining the length between the center points of two adjacent pore bodies of the throat, while subtracting the radii of the two pore bodies.

Table 2 provides the pore size statistics used for the calculations, with Cases I-3 and II-2 serving as the reference models. Case I calculations were meant to show the effects of aggregate porosity, and Case II calculations the effects of aggregate permeability. Based on the data in Table 1, the single aggregate porosity (Case I in Table 2) was varied between 0.082 and 0.700 in 6 steps by changing the aggregate pore body size distributions. The

Table 2
Minimum (R_{min}), maximum (R_{max}) and mean (R_m) pore body radii (Case I) and pore throat radii (Case II), as well as standard deviations (σ), of the pore-size distributions used in the calculations.

	Case	R_{min} (mm)	R_{max} (mm)	R_m (mm)	σ (mm)
Porosity effects	Pore body radii				
	I-1	0.0375	0.050	0.045	0.0025
	I-2	0.050	0.070	0.060	0.0030
	I-3 (Reference model)	0.055	0.075	0.065	0.0030
	I-4	0.070	0.090	0.080	0.0030
	I-5	0.075	0.100	0.090	0.0040
	I-6	0.090	0.120	0.100	0.0040
Permeability effects	Pore throat radii				
	II-1	0.001	0.010	0.005	0.0015
	II-2 (Reference model)	0.010	0.020	0.015	0.0015
	II-3	0.020	0.030	0.025	0.0015
	II-4	0.040	0.050	0.045	0.0015

aggregate throat radii as well as the macropore sizes were kept constant in these simulations to examine the effects of varying aggregate porosities on flow and transport. For the Case II simulations (Table 2), the aggregate permeability was varied by changing the aggregate throat sizes in 4 steps, while the aggregate body and macropore body/throat sizes were kept constant. Simulation II-1 had smaller throats, and simulations II-3 and II-4 larger throats, compared to the reference model (Case II-2).

The presence of macropores and aggregates with distinctly different micropore sizes created various pore systems. To explore the contribution of the different pore systems, porosities were calculated separately for the macropores and aggregates. Pore bodies were presumed to be spherically shaped, and pore throats to be cylindrical capillaries. Using the pore volumes of each domain, the domain porosities could be obtained, with the total porosity of the dual-porosity medium being simply the sum of the macropore and micropore domain porosities. For all simulations we kept the mean pore water velocity constant at a value of 1.50×10^{-5} m/s. The molecular diffusion coefficient, D_0, was set at 1.6×10^{-9} m^2/s, the viscosity at 0.001 Pa s, and the fluid density at 1 g/cm^3.

For all simulations we injected into the pore network a pulse of one pore volume (equivalent to 66 min) of a tracer having a relative concentration of 1.0. BTCs of the average concentrations as obtained with the pore network model were analysed using the CXTFIT program (Toride et al., 1995) within the STANMOD software of Šimunek et al. (2000), leading to estimates of the solute dispersivity, $\lambda = D_m/v$, the fraction of mobile water, ϕ_m, and the mass transfer coefficient, α, in Eqs. (1) and (2). This in turn also produced values of the mobile water content, θ_m, and the immobile water content, θ_{im}. The intrinsic permeability was determined for the domain as a whole, as well as for the macropore domain separately (i.e., excluding the presence of the aggregates). In addition, simulations were performed to obtain the intrinsic permeability of the single aggregates. For the Case II simulations, based on the simulated pore velocities, the characteristic time scales of diffusion and advection were calculated to explore the effects of the porewater velocity ratio between the macropore and aggregate domains on the calculations.

3. Results and discussion

Before presenting results of the various pore network calculations, we first summarize the pore network that was used for the reference simulations.

3.1. Reference model

The structured macropore network consisted of 12,929 pore throats connected to each other at 6850 junctions serving as the pore bodies, while the mean pore coordination number was 3.7. A total of 1000 aggregates were randomly placed within the macropore network. Statistics of the generated pore network are given in Table 3. The total number of pores within the created computational domain was 3,357,025. The macropore domain porosity was 0.198, and the mean porosity of the single aggregates 0.204. Fig. 2 shows the generated pore body and pore throat size distributions of the reference model, while Fig. 3 shows the generated dual-porosity pore network.

Table 3
Statistics of the generated aggregates.

Property	Value*
Number of aggregates	1000
Mean aggregate diameter (mm)	2.141 (0.475)
Aggregate pore bodies in domain	965,985
Mean pore bodies per aggregate	966 (578)*
Aggregate pore throats in domain	2,391,040
Mean pore throats per aggregate	2391 (1424)*
Mean coordination number	4.95

* Values in parenthesis indicate standard deviations.

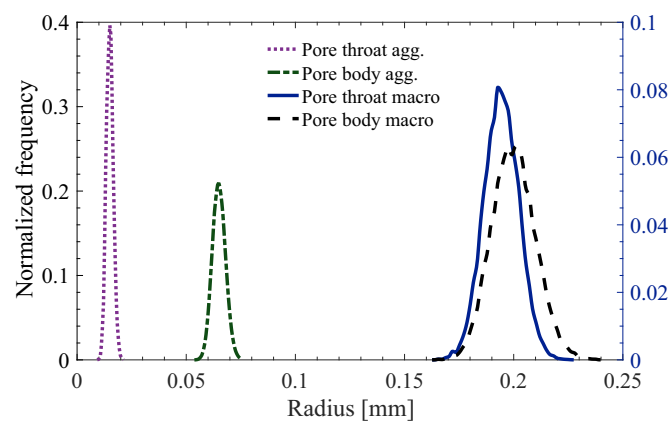

Fig. 2. Pore body (the right vertical axis) and pore throat (the left vertical axis) size distributions used for the macropore and aggregate domains of the reference model.

3.2. Case I: porosity effects

Based on the information in Table 1, six different pore body size distributions were generated as displayed in Fig. 4. Table 4 summarizes the porosities of the micropore and macropore domains for the Case I simulations. The porosity of the single aggregates ranged from very small (0.082) to very large (0.700). The aggregate domain porosity ranged from 0.013 to 0.114, and the total domain

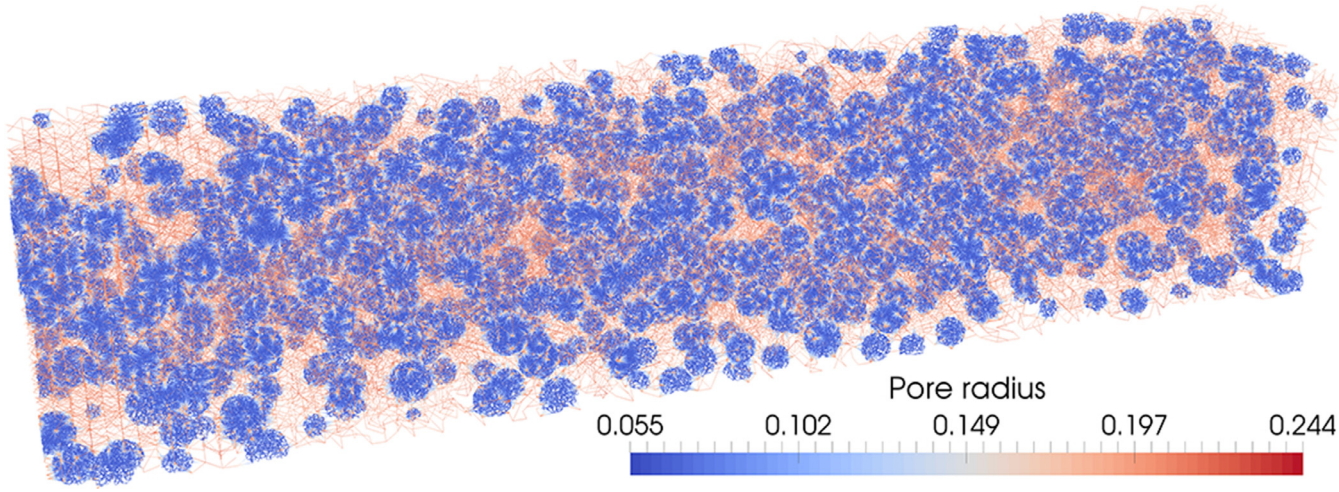

Fig. 3. Pore radii of the constructed pore network containing 1000 aggregates and composed of a total of 3,357,025 pores.

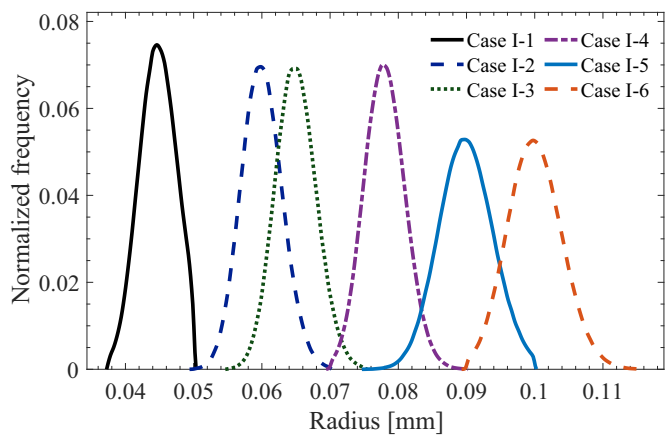

Fig. 4. Aggregate pore body size distributions for the Case I pore network calculations. The corresponding porosity values are provided in Table 4.

porosity (micropore and macropore domains combined) from 0.214 to 0.315 (the porosity of the macropore domain was kept constant at 0.198).

Fig. 5 shows the simulated solute concentration distributions for Cases I-1, I-3, and I-6 after injecting 1.0 pore volume of solute into the medium. The distributions are given at $T = 1.1$ pore volume, with pore volume defined as $T = q_t/(\phi_t L)$, where L is the length of the medium (100 mm). Concentration distributions at other times are provided in the Supplementary Material, as well a video clip showing the effect of aggregate porosity. A pulse injection was used to show both solute diffusion into the aggregate domain and subsequent back diffusion from the aggregate domain into the macropore domain. The plots in Fig. 5 show increased solute spreading as the porosity of single aggregates increased. Case I-6 with its very high single aggregate porosity ($\phi_{sa} = 0.700$) was included as a mere limiting case. The other extreme would be if no aggregate porosity were to be present ($\phi_{sa} = 0$), in which case no intra-aggregate diffusion would take place and the standard advection-dispersion equation presumably would apply.

Fig. 6 shows calculated BTCs (indicated by symbols) obtained with the pore network model at 30, 60 and 90 mm distances from the inlet for all Case I scenarios. Also included are the fitted curves obtained with the macroscopic mobile-immobile (MIM) dual-porosity model given by Eqs. (1) and (2). We optimized for this purpose the parameters (λ_m, ϕ_m and α) simultaneously to the three curves (i.e., at $x = 30$, 60 and 90 mm) obtained for each domain with a particular porosity of single aggregates. R^2 values for all Case I calculations, as well for the various Case II examples to be discussed later, were always higher than 0.9995, thus reflecting excellent descriptions of the pore-scale modelling results using the macroscopic formulation. Fig. 7 shows the fitted BTCs at 90 mm for all six scenarios. Similar BTCs at 30 and 60 mm are provided in the Supplementary Materials.

The results in Fig. 6 indicate increased spreading of the BTCs obtained at larger distances. Also, while the BTCs of Case I-1 were nearly symmetrical, Case I-6 with its highest porosity of single aggregates produced far more asymmetry and tailing in the distributions. Higher porosities of single aggregates (and hence more relatively immobile water) clearly enhanced the extent of preferential flow as exhibited by early breakthrough and late-time tailing of the curves in Fig. 7. This agrees with previous study done on highly heterogenous rocks by Mehmani et al. (2015) who showed that an increasing fraction of microporosity causes more tailing of the observed solute plume. Our findings are also consistent with several other previous studies (e.g., van Genuchten and Wierenga, 1976; Brusseau, 1993; Shukla, 2013).

Table 5 provides the transport parameters obtained for the six Case I calculations. Results indicate that a higher aggregate porosity caused a decrease in the mobile water fraction, ϕ_m, and an

Table 4
Micro- and macro-porosities for the Case I calculations with variable aggregate porosities.

	Case	Total domain porosity $\phi_t = \phi_{ag} + \phi_{macro}$	Porosity of single aggregate ϕ_{sa}	Contribution of aggregates to total porosity ϕ_{ag}/ϕ_t
Porosity effects	I-1	0.214	0.082	0.078
	I-2	0.227	0.163	0.131
	I-3	0.234	0.204	0.156
	I-4	0.260	0.362	0.239
	I-5	0.284	0.510	0.304
	I-6	0.315	0.700	0.372

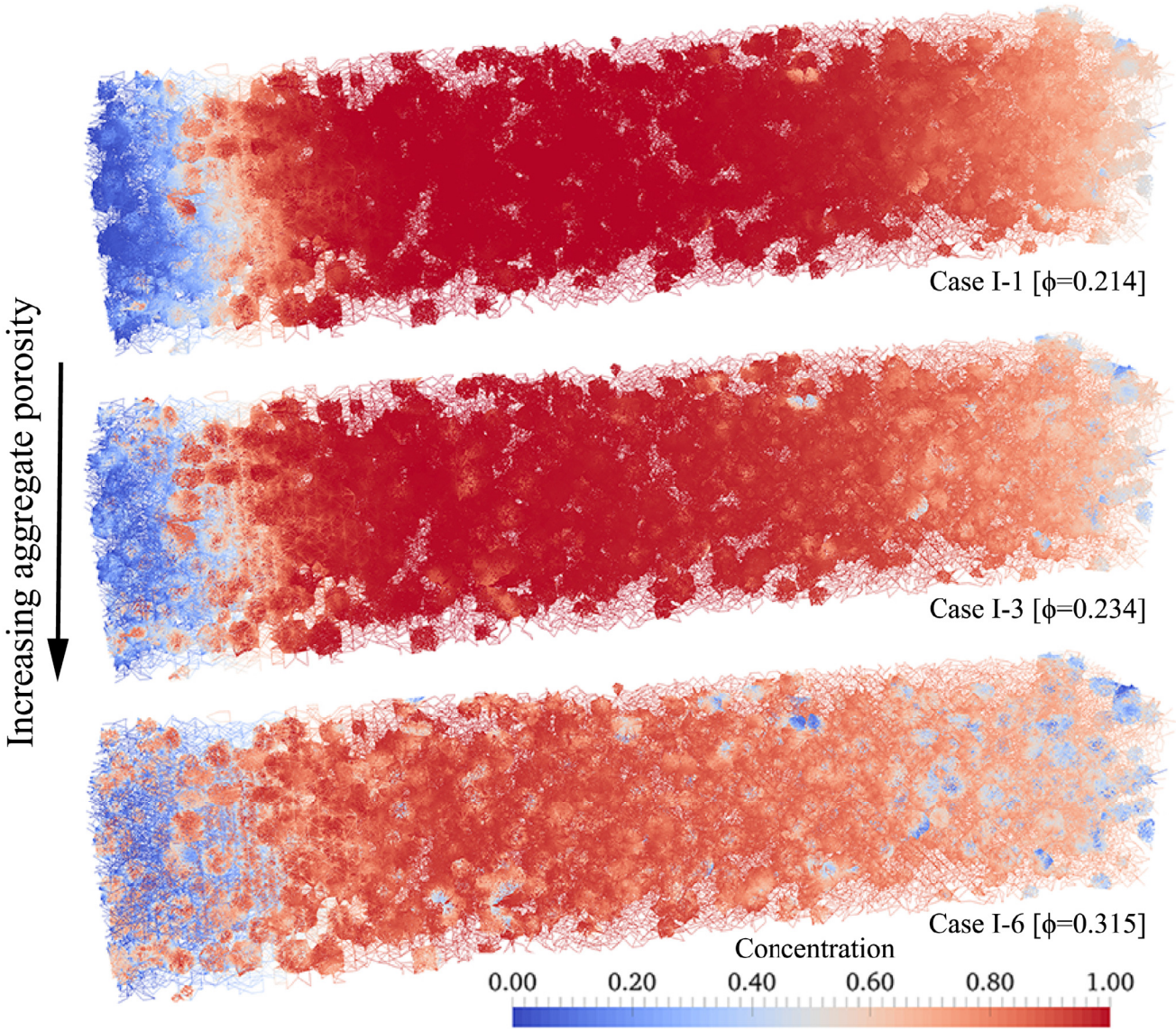

Fig. 5. Progress of advective transport and dispersion into the domain for Cases I-1, I-3 and I-6 after 1.1 pore volumes. A total of 1.0 pore volumes of tracer was injected.

increase in the mass transfer coefficient, α. The mobile water content, θ_m, was found to be approximately 0.21 for all Case I simulations, which is slightly higher than the macroporosity of 0.198. For all of the simulations, the mobile water content was slightly larger than the macro domain porosity. This is because the calculated fraction of mobile water (ϕ_m) at the macroscopic level is determined by the flow lines affected by the presence of both macropores and aggregates. Fig. 8 shows that a clear relationship exists between the mobile water content, ϕ_m, and the fraction of macropores. As compared with the porosity of macropores, the fraction of mobile water content using the fitting resulted in 5–10% larger values.

Fig. 9 shows the relationship we found between the mass transfer coefficient, α, and the porosity of single aggregates, ϕ_{sa}. The mass transfer coefficient increased with aggregate porosity as more solute mass could be transported into aggregates having higher porosity values and higher permeabilities as discussed next.

To further analyse and interpret the pore scale modelling results, we calculated the permeability (K) of the macro domain and the aggregate domain, as well as the permeability ratio between the aggregates and the macropore region (K_{agg}/K_{macro}). The permeability of the macropore domain was found to be 2.24×10^{-4} mm^2, with the results for K_{agg} and K_{ratio} given in Table 6. When the porosity of the single aggregates increased, pores come to be closer to each other, which resulted in higher aggregate permeability values and larger permeability ratios. With a larger permeability, more fluid may flow into and through the aggregates, leading to higher α and lower ϕ_m values (Fig. 10).

3.3. Case II: aggregate permeability effects

Utilizing the input parameters from Table 1, pore body size distributions were generated for the various examples. We used domains with four different pore-throat size distributions for the aggregates (Fig. 11). Flow and solute transport simulations were carried out for each pore size distribution. Note that the reference model is Case II-2, which corresponds to Case I-3 of the first set of simulations. Table 7 provides the porosity values for the Case II simulations. The data show that an increase in the pore throat radii increased the single aggregate porosity as well as the total porosity.

The progress of one pore volume of solute moving through and dispersing into the domains of Cases II-1, II-2, and II-4 at 1.1 pore

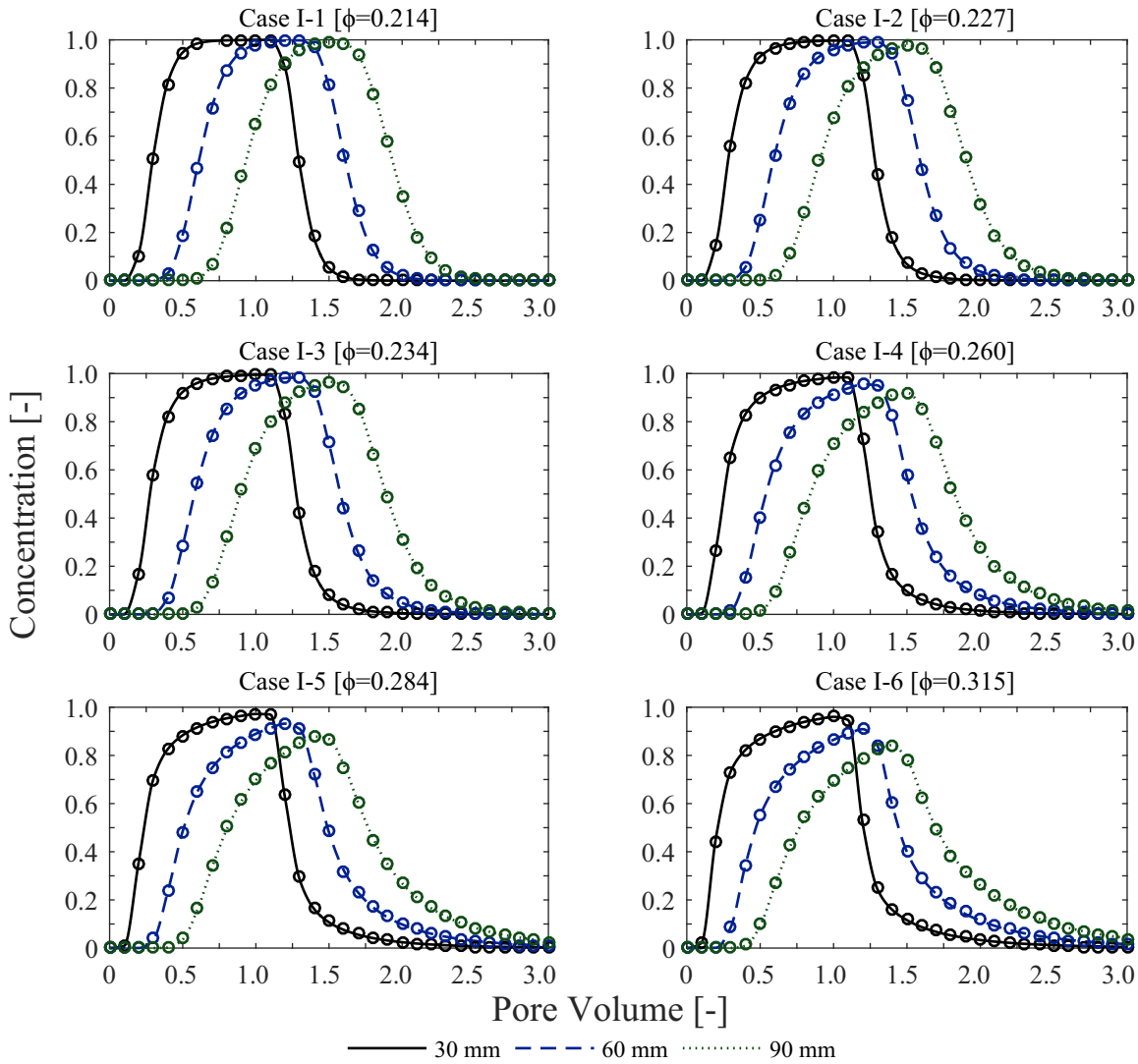

Fig. 6. Aggregate porosity effects: BTCs obtained with pore network modelling (symbols) and the fitted MIM transport BTCs (solid lines) for the Case I simulations.

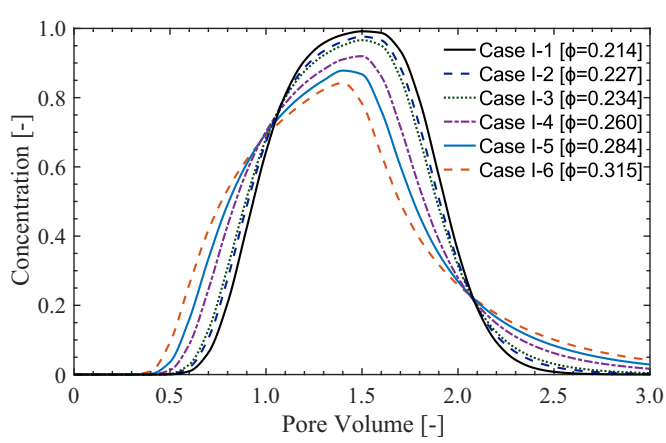

Fig. 7. BTCs obtained with the macroscopic MIM model as fitted to the pore network modelling results at 90 mm for Case I simulations.

volumes are shown in Fig. 12. Similar visualizations at multiple time levels are provided in the Supplementary Material, as well a video clip showing the effect of aggregate permeability. Flow of solute-free water after entry of the concentration pulse into the domain shows that solutes moved much faster into and through the macropore domain for Case II-4, while the residence time of solutes in the aggregates was higher for Case II-1. These results indicate that the exchange rate of the solute tracer between the aggregate and macropore domains for Case II-1 was lower than for Cases II-2 and II-4. A higher solute exchange rate was observed especially for Case II-4 due to the fact that solutes in the aggregates were almost instantly leached back into the macropore domain (also see Supplementary Material).

Table 5
Optimized MIM transport parameters for the Case I simulations.

	Case	v (mm min^{-1})	λ (mm)	ϕ_m (–)	α (min^{-1})	θ_m (–)	θ_{im} (–)
Porosity effects	I-1	1.44	1.47	0.967	1.52×10^{-5}	0.207	0.007
	I-2	1.46	1.58	0.930	1.74×10^{-5}	0.211	0.016
	I-3	1.46	1.63	0.908	2.03×10^{-5}	0.213	0.022
	I-4	1.45	1.78	0.822	3.48×10^{-5}	0.210	0.043
	I-5	1.48	1.86	0.747	3.79×10^{-5}	0.212	0.072
	I-6	1.47	1.84	0.661	4.81×10^{-5}	0.208	0.107

Fig. 13 compares the BTCs for the individual simulations, while Fig. 14 shows a comparison of the different simulations for Case II at a longitudinal distance of 90 mm. BTCs obtained at 30 and 60 mm are provided in the Supplementary Materials. The plots

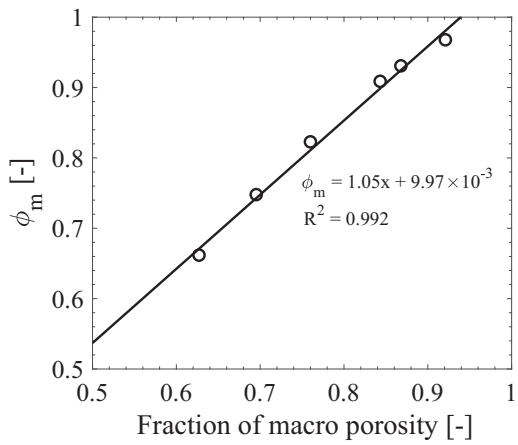

Fig. 8. Plot of the mobile water content (ϕ_m) against the fraction of macroporosity for Case I simulations. A value of 1 for ϕ_m would mean the absence of any aggregates.

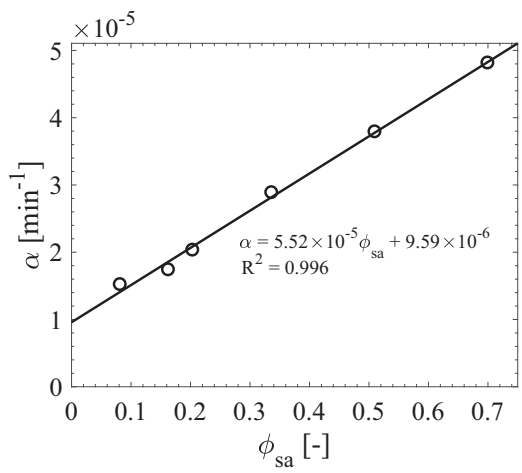

Fig. 9. Plot of the mass transfer coefficient (α) against the porosity of single aggregates (ϕ_{sa}) for Case I.

Table 6
Calculated permeability values for the aggregates, and the permeability ratio (K_{agg}/K_{macro}) for Case I.

	Case	K_{agg} (mm^2)	K_{ratio} [-]
Porosity effects	I-1	5.06×10^{-7}	2.26×10^{-3}
	I-2	1.09×10^{-6}	4.87×10^{-3}
	I-3	1.50×10^{-6}	6.71×10^{-3}
	I-4	7.25×10^{-6}	3.24×10^{-2}
	I-5	1.60×10^{-5}	7.13×10^{-2}
	I-6	2.35×10^{-5}	1.05×10^{-1}

show that reduced pore throat sizes lead to earlier breakthrough of solute, increased attenuation of the peak concentration, and more positive skewness of the BTCs in the form of tailing (e.g., Case II-1). Increasing pore throat sizes, on the other hand, resulted in delayed breakthrough curves with less tailing and more symmetrical BTCs. This is consistent with the visualizations in Fig. 12 and the Supplementary Materials, which show a more uniform solute front for Case II-4 as compared to Case II-1. The latter case exhibits more preferential flow and more pronounced tailing.

Utilizing the BTCs, transport parameters were again obtained for each simulation using the CXTFIT program. The results are given in Table 8. The obtained mobile fraction, ϕ_m, was found to be higher than the volume fraction of macropores for Cases II-1,

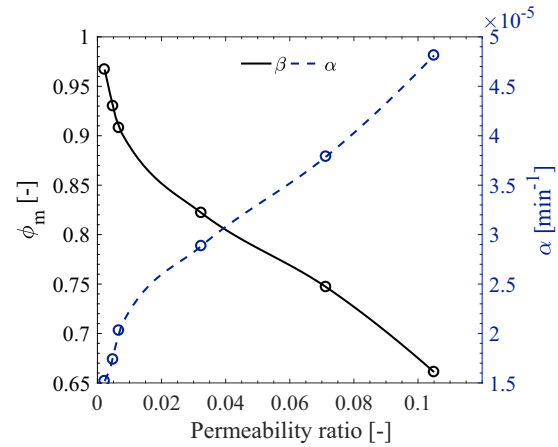

Fig. 10. Values of the mobile water fraction (ϕ_m) and the mass transfer coefficient (α) plotted against the permeability ratio (K_{agg}/K_{macro}) for Case I.

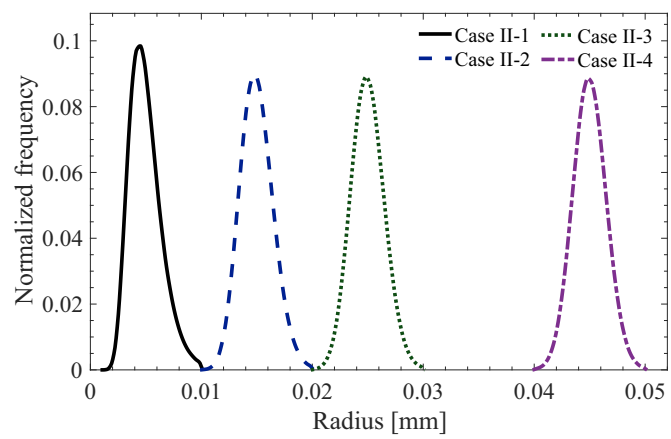

Fig. 11. Aggregate pore throat size distributions for Case II pore network calculations. The corresponding porosity values are provided in Table 7.

II-2, and II-3, while ϕ_m was lower than the volume fraction of macropores for Cases II-4. These results are due to the hydrodynamic effects caused by the presence of aggregates in the domain. Smaller pore throats create relatively impermeable aggregates, which causes the overall fluid flow path through the macropores to become more tortious, leading to higher immobile fractions at the macroscopic scale. On the other hand, the presence of aggregates with larger pore throats causes a less tortuous flow path as aggregates provide a noticeable contribution to the total flow, leading to lower immobile water fractions at the macroscopic scale. The mass transfer rate, α, was lowest for Case II-1 and highest for Case II-4. This is in agreement with our earlier observations about the visualizations.

Table 9 shows calculated pore water velocities of the macropore and micropore (aggregate) domains. The data indicate that larger pore throat sizes lead to higher pore water velocities. Fig. 15 shows plots ϕ_m and α against the velocity ratio, v_{agg}/v_{ma}. The mass transfer rate, α, decreased with a lower velocity ratio. In contrast with Case I, an increase in α did not lead to longer tailing but produced more symmetric BTCs. Increasing the aggregate pore water velocities caused the dominant transport process in the micropore domains to change from diffusion dominated to advection dominated. Interactions between the aggregate and macropore domains consequently increased, leading to higher values of the mass transfer coefficient, α. We note here that the two-region mobile-immobile model (MIM) considers the immobile domain to be completely

Table 7
Micro- and macro-porosities for the Case II calculations with variable aggregate permeability.

	Case	Total domain porosity $\phi_t = \phi_{ag} + \phi_{ma}$	Porosity of single aggregate ϕ_{sa}	Contribution of aggregates to total porosity ϕ_{ag}/ϕ_t
Permeability effects	II-1	0.229	0.193	0.137
	II-2	0.234	0.202	0.141
	II-3	0.242	0.219	0.147
	II-4	0.272	0.281	0.166

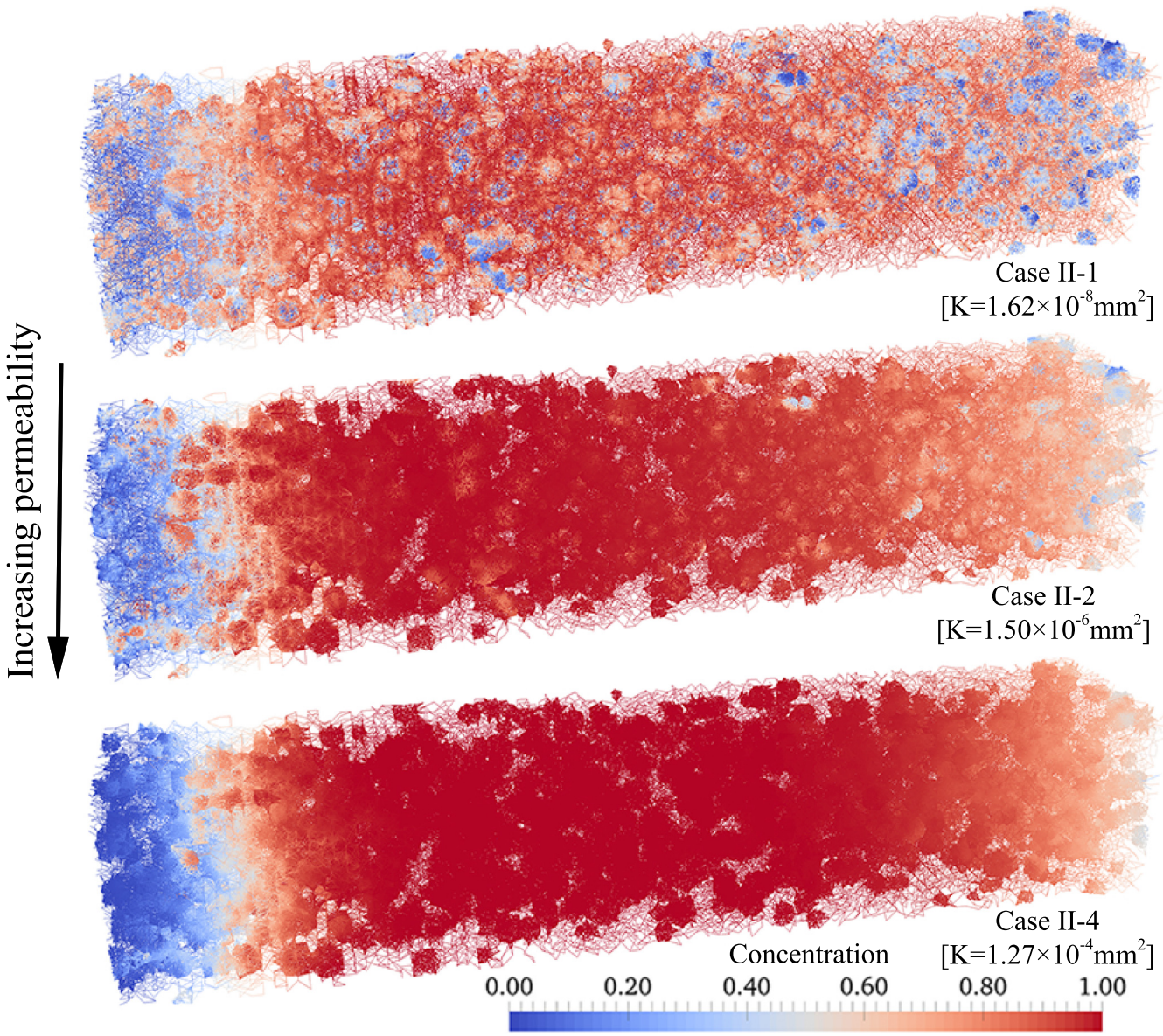

Fig. 12. Progress of advective transport and dispersion into the domains of Cases II-1, II-2, and II-4 after 1.1 pore volumes. A total of 1.0 pore volumes of tracer was injected.

diffusion dominated, which likely contributed to the fluctuations in ϕ_m with the velocity ratio.

When solute-free water is injected and the transport regime in the aggregate domain is diffusion dominated, then the characteristic time for solutes to diffuse back into the macropore domain is given by $t_{dif} = l^2/D_m$, where l is the effective length of the aggregates and D_m the molecular diffusion coefficient. For an advection dominated transport regime, on the other hand, the characteristic transport time is described by $t_{adv} = l/\bar{v}$, where l is now the domain length. These time scales are characteristic for the extent of BTC tailing when the amount of mass stored in the aggregates is noticeable, and when the velocity ratio is low. The advection and diffusion time scales for the aggregate and macropore domains are listed in Table 10. For these calculations we used the mean fluid velocity in the pore bodies and throats, while for the characteristic length of the aggregates we used the mean aggregate radius.

We used the transport time scales to identify the dominant transport mechanism in the aggregate domain. When $t_{adv,agg} < t_{dif,agg}$, transport in the aggregate domain is primarily advection dominated, but when $t_{adv,agg} > t_{dif,agg}$ the aggregated domain becomes more dominated by diffusion. The data in Table 10 indicate that Case II-1 was very much diffusion dominated, while the experiments towards Case II-4 became increasingly more advection dominated. Tailing will be observed when the characteristic time

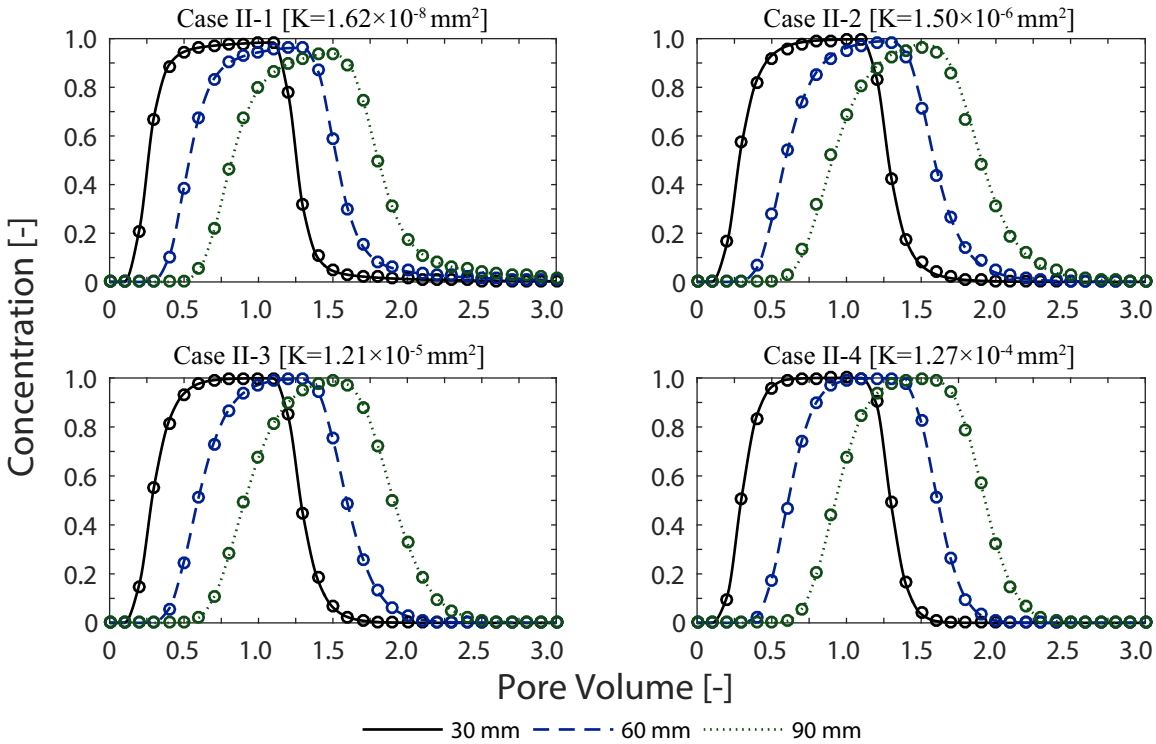

Fig. 13. Aggregate permeability effects: BTCs obtained with pore network modelling (symbols) and the fitted MIM transport BTCs (solid lines) for the Case II simulations.

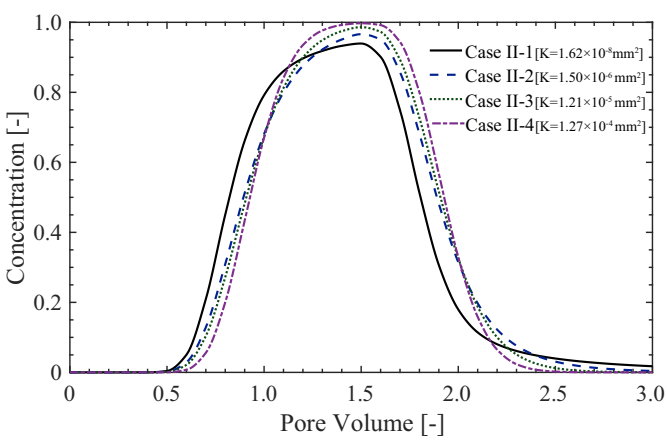

Fig. 14. BTCs obtained with the macroscopic MIM model as fitted to the pore network modelling results at 90 mm for Case II.

for diffusive transport in the aggregates is similar or becomes less in comparison to the advection time scale in the macropore domain.

For Case II-1, when the transport domain is leached, the amount of solute tracer remains relatively high in the micropore domain since the time of solute tracer to be transported back into the macropore domain is much lower than the front of the solute-free water passing through the domain. This effect becomes less visible for Case II-2, and is almost absent for Case II-4. Extensive tailing is observed when the transport regime in the aggregates is diffusion dominated and the transport regime in the macro domain is advection dominated. For flow conditions when the velocity ratio between the two domains is close to 1, fluid passes through the aggregates as well as through the macropore domain, leading to relatively symmetrical BTCs. Fluid flow at lower velocity ratios is relatively much slower in the aggregates, leading to long tails in the BTC. These findings agree with other studies, such as those by Brusseau (1993) and Bijeljic et al. (2013), who found that the degree of non-equilibrium and dominance of the velocity variations between the inter-aggregate and intra-aggregate pores influence the severity of tailing.

Values of the calculated permeabilities are listed in Table 11. With increasing pore throat sizes, the permeability increased, with the permeability ratio increasing from a value of 7.24×10^{-5} for Case II-1 to 0.56 for Case II-4. This means that for Case II-4 the fluid penetrated into aggregates almost as easy as it passed through the macropores. For Case II-1 the ratio is very low, meaning that fluid flow now takes place much less through the aggregate pores as compared to the macropores. This is consistent with the fact that considerable tailing was observed in the BTCs of Case II-1, while Case II-4 produced more symmetrical BTCs.

Table 8
Optimized MIM transport parameters for the Case II simulations.

	Case	v (mm min^{-1})	λ (mm)	ϕ_m (–)	α (min^{-1})	θ_m (–)	θ_{im} (–)
Permeability effects	II-1	1.51	1.47	0.891	7.31×10^{-6}	0.204	0.025
	II-2	1.46	1.63	0.908	2.03×10^{-5}	0.212	0.021
	II-3	1.46	1.37	0.878	6.93×10^{-5}	0.213	0.030
	II-4	1.46	1.24	0.789	1.27×10^{-3}	0.215	0.057

Table 9
Mean pore water velocities in the macropore and aggregated domains for Case II.

		Pore bodies (mm min^{-1})			Pore throats (mm min^{-1})		
	Case	v_{agg}	v_m	$v_{agg/m}$	v_{agg}	v_m	$v_{agg/m}$
Permeability effects	II-1	2.32×10^{-4}	5.40	4.30×10^{-5}	1.51×10^{-2}	2.99	5.05×10^{-3}
	II-2	1.67×10^{-2}	5.48	3.05×10^{-3}	1.19×10^{-1}	3.04	3.92×10^{-2}
	II-3	1.24×10^{-1}	5.58	2.22×10^{-2}	3.19×10^{-1}	3.09	1.03×10^{-1}
	II-4	1.02	5.79	1.75×10^{-1}	8.06×10^{-1}	3.10	2.60×10^{-1}

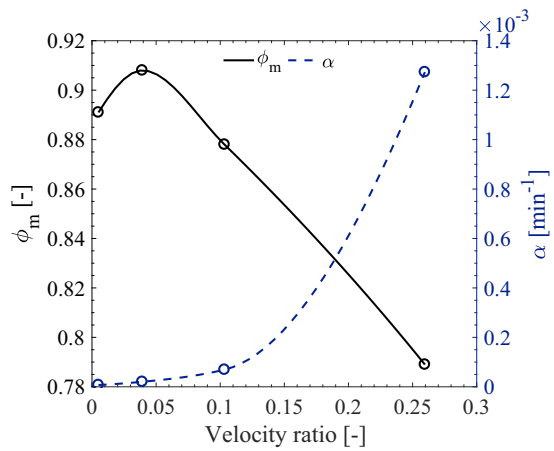

Fig. 15. Values of the mobile water fraction (ϕ_m) and the mass transfer coefficient (α) plotted against the velocity ratio (v_{agg}/v_{ma}) for Case II.

Table 10
Characteristic advection and diffusion times (in minutes) for the Case II simulations.

	Case	$t_{adv,ma}$	$t_{adv,agg}$	$t_{dif,agg}$	Transport regime
Permeability effects	II-1	23.86	139.69	19.10	Diffusive
	II-2	23.49	15.77	19.10	Advective
	II-3	23.08	4.83	19.10	Advective
	II-4	22.48	1.18	19.10	Advective

Table 11
Calculated permeability values for the aggregates, and the permeability ratio (K_{agg}/K_{macro}) for Case II.

	Case	K (mm^2)	K_{ratio} (-)
Permeability effects	I-1	1.62×10^{-8}	7.24×10^{-5}
	I-2	1.50×10^{-6}	6.71×10^{-3}
	I-3	1.21×10^{-5}	5.40×10^{-2}
	I-4	1.27×10^{-4}	5.65×10^{-1}

4. Conclusions

We investigated the effects of multi-scale pore sizes in a dual-porosity porous medium on fluid flow and solute transport processes. Several dual-porosity pore networks were constructed by placing a large number of aggregates into the macropore domain. After construction of the aggregate domains, fluid flow and solute transport were simulated using the PoreFlow (Raoof et al., 2013) pore network model to obtain three-dimensional flow fields and solute distributions, as well as the BTCs at several locations along the flow path. The resulting BTCs were fitted analysed in terms of the conventional macroscopic dual-porosity (MIM) transport model to estimate several key macroscopic transport parameters. Use of pore scale modelling provided information to link the transport properties to the underlying pore scale processes, which would be very difficult and time-consuming to do using only experimental methods.

A pore network model consisting of 1000 aggregates, each having an average of 966 intra-aggregate pores, was generated to produce a domain with total of 3,357,025 pores. By varying the pore sizes, different aggregates with porosity values between 0.082 and 0.700 were obtained. We showed that increasing aggregate porosities did lead to higher values of the mass transfer coefficient and more tailing in the BTCs. Higher fluid velocities within the aggregate domain also increased the mass transfer coefficient, but produced less tailing in the calculated BTCs. On the other hand, lower pore water velocities in the micropore domain produced lower mass transfer coefficients but more extensive tailing in the BTCs. The velocity ratio between the aggregated and macro domain could explain the magnitude of tailing observed in the BTCs.

We showed that dual-porosity pore network models are attractive tools for investigating the basic processes governing solute interactions between the macropore domain (containing interaggregate pores) and the micropore or aggregate domain (containing intra-aggregate pores). The developed pore network model provides a flexible means of analysing the effects of pore scale transport properties such as aggregate porosity and permeability on macroscopic flow and transport parameters of dual-porosity porous media.

While in this study we focused on the effects of aggregate porosity and permeability on macroscopic transport, further studies are needed to better understand all of the pore scale properties of aggregates. In our work we varied the aggregate porosity by varying the size of the pore bodies. The aggregate porosity can vary also as a result of changes in the number of pore bodies, the pore coordination number, and the size of the throats. The influence of the range, variance, skewness, and curtosis of the pore size distribution on the mass transfer coefficients must also be investigated further. We note also that aggregate domain porosity can be influenced by the size and number of aggregates, which have been kept constant in this study. We furthermore did not consider any direct connections between the aggregates. These connections will have an influence on the residence time of the solute in the aggregated domain. They very likely will influence the magnitude of transferred mass, and how solutes are exchanged between the micropore and macropore domains. The use of suitable imaging techniques remains indispensable in all of this to most accurately obtain the exact micropore structures of the aggregates, and the porous medium as a whole.

Acknowledgements

This work is part of the Veni Talent Scheme awarded to A. Raoof with project number 016.151.047, which is (partly) financed by the Netherlands Organisation for Scientific Research (NWO).

Supplementary materials

Supplementary material associated with this article can be found, in the online version, at doi:10.1016/j.advwatres.2017.04.013.

References

Abbaspour, K.C., Kohler, A., Šimunek, J., Fritsch, M., Schulin, R., 2001. Application of a two-dimensional model to simulate flow and transport in a macroporous agricultural soil with tile drains. Eur. J. Soil Sci. 52, 433–447. http://dx.doi.org/10.1046/j.1365-2389.2001.00389.x.

Allaire, S.E., Roulier, S., Cessna, A.J., 2009. Quantifying preferential flow in soils: a review of different techniques. J. Hydrol. 378, 179–204. http://dx.doi.org/10.1016/j.jhydrol.2009.08.013.

Barker, J.A., 1985. Block-geometry functions characterizing transport in densely fissured media. J. Hydrol. 77, 263–279.

Bolt, G.H., 1979. Movement of solutes in soil: principles of adsorption/exchange chromatography. In: Bolt, G.H. (Ed.), Soil Chemistry, B. Physico-Chemical Models. Developments in Soil Science 5B. Elsevier, Amsterdam, pp. 295–348.

Bijeljic, B., Mostaghimi, P., Blunt, M.J., 2013. Insights into non-Fickian solute transport in carbonates. Water Resour. Res. 49 (5), 2714–2728. http://dx.doi.org/10.1002/wrcr.20238.

Brusseau, M.L., 1993. The influence of solute size, pore water velocity, and intraparticle porosity on solute dispersion and transport in soil. Water Resour. Res. 29 (4), 1071–1080.

Bultreys, T., Van Hoorebeke, L., Cnudde, V., 2015. Multi-scale, micro-computed tomography-based pore network models to simulate drainage in heterogeneous rocks. Adv. Water Resour. 78, 36–49. http://dx.doi.org/10.1016/j.advwatres.2015.02.003.

Bultreys, T., De Boever, W., Cnudde, V., 2016. Imaging and image-based fluid transport modeling at the pore scale in geological materials: a practical introduction to the current state-of-the-art. Earth-Sci. Rev. 155, 93–128. http://dx.doi.org/10.1016/j.earscirev.2016.02.001.

Cnudde, V., Boone, M.N., 2013. High-resolution X-ray computed tomography in geosciences: a review of the current technology and applications. Earth-Sci. Rev. 123, 1–17. http://dx.doi.org/10.1016/j.earscirev.2013.04.003.

Czachor, H., Charytanowicz, M., Gonet, S., Niewczas, J., Jozefaciuk, G., Lichner, L., 2015. Impact of long-term mineral and organic fertilizer application on the water stability, wettability and porosity of aggregates obtained from two loamy soils. Eur. J. Soil Sci. 66 (3), 577–588. http://dx.doi.org/10.1111/ejss.12242.

Clothier, B.E., Kirkham, M.B., McLean, J.E., 1992. In situ measurements of the effective transport volume of solute moving through soil. Soil Sci. Soc. Am J. 56, 733–736.

Coats, K.H., Smith, B.D., 1964. Dead end pore volume and dispersion in porous media. Soc. Petrol. Eng. J. 4, 73–84.

Dal Ferro, N., Berti, A., Francioso, O., Ferrari, E., Matthews, G.P., Morari, F., 2012. Investigating the effects of wettability and pore size distribution on aggregate stability: the role of soil organic matter and the humic fraction. Eur. J. Soil Sci. 63 (2), 152–164. http://dx.doi.org/10.1111/j.1365-2389.2012.01427.x.

Dal Ferro, N., Charrier, P., Morari, F., 2013. Dual-scale micro-CT assessment of soil structure in a long-term fertilization experiment. Geoderma 204, 84–93. http://dx.doi.org/10.1016/j.geoderma.2013.04.012.

Fathi, H., Raoof, A., Mansouri, S.H., van Genuchten, M.T., 2017a. Effects of porosity and water saturation on the effective diffusivity of a cathode catalyst layer. J. Electrochem. Soc. 164 (4), F298–F305. http://dx.doi.org/10.1149/2.0871704jes.

Fathi, H., Raoof, A., Mansouri, S.H., 2017b. Insights into the role of wettability in cathode catalyst layer of proton exchange membrane fuel cell; pore scale immiscible flow and transport processes. J. Power Sources 346, 57–67. http://dx.doi.org/10.1016/j.jpowsour.2017.03.012.

Flury, M., Flühler, H., Jury, W.A., Leuenberger, J., 1994. Susceptibility of soils to preferential flow of water: a field study. Water Resour. Res. 30, 1945–1954.

Gerke, H.H., 2006. Preferential flow descriptions for structured soils. J. Plant Nutr. Soil Sci. 169, 382–400. http://dx.doi.org/10.1002/jpln.200521955.

Goltz, M.N., Roberts, P.V., 1987. Using the method of moments to analyze three-dimensional diffusion-limited solute transport from temporal and spatial perspectives. Water Resour. Res. 23 (8), 1575–1585.

Hantush, M.M., Mariño, M.A., 1988. Interlayer diffusive transfer and transport of contaminants in stratified formation. I. Theory. J. Hydrogeol. Eng., ASCE. 3 (4), 232–240.

Hendrickx, J.M.H., Flury, M., 2001. Uniform and preferential flow mechanisms in the vadose zone. In: Conceptual Models of Flow and Transport in the Fractured Vadose Zone. National Research Council, National Academy Press, Washington, DC, pp. 149–187.

Hemes, S., Desbois, G., Urai, J.L., Schröppel, B., Schwarz, J.O., 2015. Multi-scale characterization of porosity in Boom Clay (HADES-level, Mol, Belgium) using a combination of X-ray μ-CT, 2D BIB-SEM and FIB-SEM tomography. Microporous Mesoporous Mater. 208, 1–20. http://dx.doi.org/10.1016/j.micromeso.2015.01.022.

Hillel, D., 2003. Introduction to Environmental Soil Physics. Academic Press.

Jafari, S., Yamamoto, R., Rahnama, M., 2011. Lattice-Boltzmann method combined with smoothed-profile method for particulate suspensions. Phys. Rev. E. 83 (2). http://dx.doi.org/10.1103/PhysRevE.83.026702.

Jarvis, N.J., 2007. A review of nonequilibrium water flow and solute transport in soil macropores: principles, controlling factors and consequences for water quality. Eur. J. Soil Sci. 58, 523–546. http://dx.doi.org/10.1111/j.1365-2389.2007.00915.x.

Jaynes, D.B., Shao, M., 1999. Evaluation of a simple technique for estimating two–domain transport parameters. Soil Sci. 164, 82–91.

Jiang, Z., Dijke, M.I.J., Sorbie, K.S., Couples, G.D., 2013. Representation of multiscale heterogeneity via multiscale pore networks. Water Resour. Res. 49 (9), 5437–5449. http://dx.doi.org/10.1002/wrcr.20304.

Khan, F., Enzmann, F., Kersten, M., Wiegmann, A., Steiner, K., 2012. 3D simulation of the permeability tensor in a soil aggregate on basis of nanotomographic imaging and LBE solver. J. Soils Sediments 12 (1), 86–96. http://dx.doi.org/10.1007/s11368-011-0435-3.

Köhne, J.M., Köhne, S.K., Šimůnek, J., 2009. A review of model applications for structured soils: a) Water flow and tracer transport. J. Contam. Hydrol. 104, 4–35. http://dx.doi.org/10.1016/j.jconhyd.2008.10.002.

Mahmoodlu, M.G., Hartog, N., Hassanizadeh, S.M., Raoof, A., 2013. Oxidation of volatile organic vapours in air by solid potassium permanganate. Chemosphere 91 (11), 1534–1538. http://dx.doi.org/10.1016/j.chemosphere.2012.12.035.

Mahmoodlu, M.G., Hassanizadeh, S.M., Hartog, N., Raoof, A., 2014. Oxidation of trichloroethylene, toluene, and ethanol vapors by a partially saturated permeable reactive barrier. J. Contam. Hydrol. 164, 193–208. http://dx.doi.org/10.1016/j.jconhyd.2014.05.013.

Mangalassery, S., Sjögersten, S., Sparkes, D.L., Sturrock, C.J., Mooney, S.J., 2013. The effect of soil aggregate size on pore structure and its consequence on emission of greenhouse gases. Soil Till. Res. 132, 39–46. http://dx.doi.org/10.1016/j.still.2013.05.003.

Maraqa, M.A., 2001. Prediction of mass-transfer coefficient for solute transport in porous media. J. Contam. Hydrol. 53, 163–171. http://dx.doi.org/10.1016/S0169-7722(01)00107-3.

Martínez, F.S.J., Ortega, F.M., Monreal, F.C., Kravchenko, A.N., Wang, W., 2015. Soil aggregate geometry: measurements and morphology. Geoderma 237, 36–48. http://dx.doi.org/10.1016/j.geoderma.2014.08.003.

Mehmani, A., Prodanović, M., 2014. The effect of microporosity on transport properties in porous media. Adv. Water Resour. 63, 104–119. http://dx.doi.org/10.1016/j.advwatres.2013.10.009.

Mehmani, A., Mehmani, Y., Prodanović, M., Balhoff, M., 2015. A forward analysis on the applicability of tracer breakthrough profiles in revealing the pore structure of tight gas sandstone and carbonate rocks. Water Resour. Res. 51 (6), 4751–4767. http://dx.doi.org/10.1002/2015WR016948.

NRC, 2001. Conceptual Models of Flow and Transport in the Fractured Vadose Zone. National Research Council, National Academy Press, Washington, DC.

Parker, J.C., Valocchi, A.J., 1986. Constraints on the validity of equilibrium and first-order kinetic transport models in structured soils. Water Resour. Res. 22 (3), 399–407.

Peth, S., Horn, R., Beckmann, F., Donath, T., Fischer, J., Smucker, A.J.M., 2008. Three-dimensional quantification of intra-aggregate pore-space features using synchrotron-radiation-based microtomography. Soil Sci. Soc. Am. J. 72 (4), 897–907. http://dx.doi.org/10.2136/sssaj2007.0130.

Pontedeiro, E.M., van Genuchten, M.Th., Cotta, R.M., Šimůnek, J., 2010. The effects of preferential flow and soil texture on risk assessments of a NORM waste disposal site. J. Hazard. Mater 174, 648–655. http://dx.doi.org/10.1016/j.jhazmat.2009.09.100.

Prodanović, M., Mehmani, A., Sheppard, A.P., 2015. Imaged-based multiscale network modelling of microporosity in carbonates. Geol. Soc. Lond. Special Publications 406 (1), 95–113. http://dx.doi.org/10.1144/SP406.9.

Rabbi, S.F., Wilson, B.R., Lockwood, P.V., Daniel, H., Young, I.M., 2015. Aggregate hierarchy and carbon mineralization in two Oxisols of New South Wales, Australia. Soil Till. Res. 146, 193–203. http://dx.doi.org/10.1016/j.still.2014.10.008.

Raoof, A., Hassanizadeh, S.M., 2010. A new method for generating pore-network models of porous media. Transp. Porous Media 81 (3), 391–407. http://dx.doi.org/10.1007/s11242-009-9412-3.

Raoof, A., Hassanizadeh, S.M., Leijnse, A., 2010. Upscaling transport of adsorbing solutes in porous media: pore-network modeling. Vadose Zone J. 9 (3), 624–636. http://dx.doi.org/10.2136/vzj2010.0026.

Raoof, A., Hassanizadeh, S.M., 2012. A new formulation for pore-network modeling of two-phase flow. Water Resour. Res. 48 (1). http://dx.doi.org/10.1029/2010WR010180.

Raoof, A., Hassanizadeh, S.M., 2013. Saturation-dependent solute dispersivity in porous media: pore-scale processes. Water Resour. Res. 49 (4), 1943–1951. http://dx.doi.org/10.1002/wrcr.20152.

Raoof, A., Nick, H.M., Hassanizadeh, S.M., Spiers, C.J., 2013. PoreFlow: a complex pore-network model for simulation of reactive transport in variably saturated porous media. Comp. Geosci. 61, 160–174. http://dx.doi.org/10.1016/j.cageo.2013.08.005.

Rasmuson, A., Neretnieks, I., 1980. Exact solution of a model for diffusion in particles and longitudinal dispersion in packed beds. Am. Inst. Chem. Eng. J. 26, 686–690.

Sahimi, M., 2011. Flow and Transport in Porous Media and Fractured Rock: From Classical Methods to Modern Approaches. Wiley-VCH. http://dx.doi.org/10.1002/9783527636693.

Shukla, M.K., 2013. Soil Physics: An Introduction. CRC Press.

Šimůnek, J., Jarvis, N.J., van Genuchten, M.Th., Gärdenäs, A., 2003. Review and comparison of models for describing non-equilibrium and preferential flow and transport in the vadose zone. J. Hydrol. 272 (1), 14–35. http://dx.doi.org/10.1016/S0022-1694(02)00252-4.

Šimunek, J., van Genuchten, M.Th., Šejna, M., Toride, N., Leij, F.J., 2000. The STANMOD computer software for evaluating solute transport in porous media using analytical solutions of convection-dispersion equation. In: Version 2.0, *IGWMC-TPS-71*, Int. Ground Water Modeling Center (IGWMC). Colorado School of Mines, Golden, Colorado, p. 32.

Šimunek, J., van Genuchten, M.Th, 2008. Modeling nonequilibrium flow and transport processes using HYDRUS. Vadose Zone J. 7 (2), 782–797. http://dx.doi.org/10.2136/vzj2007.0074.

Sudicky, E.A., Frind, E.O., 1982. Contaminant transport in fractured porous media: analytical solutions for a system of parallel fractures. Water Resour. Res. 18 (6), 1634–1642.
Tang, D.H., Frind, E.O., Sudicky, E.A., 1981. Contaminant transport in fractured porous media: analytical solution for a single fracture. Water Resour. Res. 17, 555–564.
Tisdall, J.M., Oades, J., 1982. Organic matter and water-stable aggregates in soils. J. Soil Sci. 33 (2), 141–163.
Toride, N., Leij, F.J., van Genuchten, M.Th, 1995. The CXTFIT code for estimating transport parameters from laboratory or field tracer experiments. In: Version 2.10. U.S. Salinity Laboratory. USDA-ARS, Riverside, CA, p. 121.
Vasilyev, L., Raoof, A., Nordbotten, J.M., 2012. Effect of mean network coordination number on dispersivity characteristics. Transp. Porous Media 95 (2), 447–463. http://dx.doi.org/10.1007/s11242-012-0054-5.
van Genuchten, M.Th., Dalton, F.N., 1986. Models for simulating salt movement in aggregated field soils. Geoderma 38 (1), 165–183.
van Genuchten, M.Th, 1985. General approach for modeling solute transport in structured soils. Memoires Int. Assoc. Hydrogeol. 17 (2), 513–526.
van Genuchten, M.Th., Wierenga, P.J., 1976. Mass transfer studies in sorbing porous media, I. Analytical solutions. Soil Sci. Soc. Am. J. 40 (4), 473–480.
van Genuchten, M.Th., Tang, D.H., Guennelon, R., 1984. Some exact solutions for solute transport through soils containing large cylindrical macropores. Water Resour. Res. 20 (3), 335–346.
Vogel, T., Sanda, M., Dusek, J., Dohnal, M., Votrubova, J., 2010. Using oxygen-18 to study the role of perefential flow in the formation of hillslope runoff. Vadose Zone J. 9, 252–259. http://dx.doi.org/10.2136/vzj2009.0066.
Wildenschild, D., Sheppard, A.P., 2013. X-ray imaging and analysis techniques for quantifying pore-scale structure and processes in subsurface porous medium systems. Adv. Water Resour. 50, 217–246. http://dx.doi.org/10.1016/j.advwatres.2012.07.018.
Zhang, Q., Hassanizadeh, S.M., Karadimitriou, N.K., Raoof, A., Liu, B., Kleingeld, P.J., Imhof, A., 2013. Retention and remobilization of colloids during steady-state and transient two-phase flow. Water Resour. Res. 49 (12), 8005–8016. http://dx.doi.org/10.1002/2013WR014345.
Zhou, H., Peng, X., Perfect, E., Xiao, T., Peng, G., 2013. Effects of organic and inorganic fertilization on soil aggregation in an Ultisol as characterized by synchrotron based X-ray micro-computed tomography. Geoderma 195, 23–30. http://dx.doi.org/10.1016/j.geoderma.2014.08.003.
Zhou, B.B., Li, Y., Wang, Q., Jiang, Y.L., Li, S., 2014. Simulation of chloride transport in an aggregated soil using three conceptual models. Arab. J. Geosci. 7 (7), 2539–2546. http://dx.doi.org/10.1007/s12517-013-0970-x.